LJMU Research Online

Pan, X, Zhang, Q, Qiu, K, Paré, DM, Chuss, DT, Butterfield, NO, Tress, RG, Sormani, MC, Tang, Y, Longmore, SN and Pillai, T

 Parallel Alignments between Magnetic Fields and Dense Structures in the Central Molecular Zone

https://researchonline.ljmu.ac.uk/id/eprint/27294/

Article

For more information please contact researchonline@ljmu.ac.uk

Parallel Alignments between Magnetic Fields and Dense Structures in the Central Molecular Zone

Xing Pan[1,2,3] , Qizhou Zhang[3] , Keping Qiu[1,2] , Dylan M. Paré[4] , David T. Chuss[4] , Natalie O. Butterfield[5] ,
Robin G. Tress[6] , Mattia C. Sormani[7] , Yuping Tang[8] , Steven N. Longmore[9,10] , and Thushara Pillai[11]

[1] School of Astronomy and Space Science, Nanjing University, 163 Xianlin Avenue, Nanjing 210023, People's Republic of China
[2] Key Laboratory of Modern Astronomy and Astrophysics (Nanjing University), Ministry of Education, Nanjing 210023, People's Republic of China
[3] Center for Astrophysics |Harvard & Smithsonian, 60 Garden Street, Cambridge, MA 02138, USA
[4] Department of Physics, Villanova University, 800 E. Lancaster Avenue, Villanova, PA 19085, USA
[5] National Radio Astronomy Observatory, 520 Edgemont Road, Charlottesville, VA 22903, USA
[6] Institute of Physics, Laboratory for Galaxy Evolution and Spectral Modeling, EPFL, Observatoire de Sauverny, Chemin Pegasi 51, 1290 Versoix, Switzerland
[7] Università dell'Insubria, via Valleggio 11, 22100 Como, Italy
[8] Shanghai Key Lab for Astrophysics, Shanghai Normal University, Shanghai 200234, People's Republic of China
[9] Astrophysics Research Institute, Liverpool John Moores University, 146 Brownlow Hill, Liverpool L3 5RF, UK
[10] Cosmic Origins Of Life (COOL) Research DAO, Germany
[11] Haystack Observatory, Massachusetts Institute of Technology, 99 Millstone Road, Westford, MA 01886, USA

Abstract

The recent Far-Infrared Polarimetric Large-Area Central Molecular Zone Exploration (FIREPLACE) survey with SOFIA has mapped plane-of-sky magnetic field orientations within the Central Molecular Zone (CMZ) of the Milky Way. Applying the Histogram of Relative Orientations analysis to the FIREPLACE data, we find that the relative orientation between magnetic fields and column density structures is random in low-density regions ($2 \times 10^{22} \lesssim N_{H_2} \lesssim 10^{23}\,\mathrm{cm^{-2}}$) but becomes preferentially parallel in high-density regions ($\gtrsim 10^{23}\,\mathrm{cm^{-2}}$). This trend is in contrast with that of the nearby molecular clouds, where the relative orientation transitions from parallel to perpendicular with increasing column densities. However, the relative orientation varies between individual CMZ clouds. Comparisons with magnetohydrodynamic simulations specific to the CMZ conditions suggest that the observed parallel alignment is intrinsic, rather than artifacts caused by the projection effect. The origin of this parallel configuration may arise from the fact that most dense structures in the CMZ are not self-gravitating, as they are in supervirial states, except for the ministarburst region Sgr B2. These findings are consistent with the low star formation efficiency observed in the CMZ compared to that in the Galactic disk.

1. Introduction

The Central Molecular Zone (CMZ) is the innermost 150 pc of our Galaxy, harboring a significant reservoir of molecular gas ($(2–6) \times 10^7\,M_\odot$; M. Morris & E. Serabyn 1996) with high surface densities ($\sim 10^{23}\,\mathrm{cm^{-2}}$ from S. N. Longmore et al. 2013; C. Battersby et al. 2024). Several massive molecular clouds, with gas mass over $10^5\,M_\odot$, have been identified in the CMZ, including well-known regions such as Sgr B2, G0.253 +0.016, Sgr C, and the Dust Ridge (P. F. Goldsmith et al. 1990; S. Huettemeister et al. 1995; S. N. Longmore et al. 2012; S. Kendrew et al. 2013; D. L. Walker et al. 2018; X. Lu et al. 2019b, 2019a). Meanwhile, the CMZ contains an extreme star-forming environment, distinct from that of the Galactic disk. M. Heyer & T. M. Dame (2015) investigated the size–line width relation in molecular gas and found that the turbulent energy in the CMZ is significantly higher than that in the Galactic disk, indicating that gas in the CMZ is more turbulent than in the disk. Additionally, the CMZ is characterized with strong magnetic fields, with mean field strengths ranging from 0.1 to 10 mG (T. Pillai et al. 2015; A. Mangilli et al. 2019; X. Lu et al. 2024; X. Pan et al. 2024).

Despite the large amount of molecular gas, the present star formation rates (SFRs) of $\simeq 0.07\,M_\odot\,\mathrm{yr^{-1}}$ for the CMZ are an order of magnitude lower than that expected from the dense gas–star formation relations (C. J. Lada et al. 2010; S. N. Longmore et al. 2013; A. T. Barnes et al. 2017; J. Kauffmann et al. 2017; X. Lu et al. 2019b). Some studies proposed that the high turbulent pressure may increase the density threshold for star formation and hence decrease the SFR (e.g., J. M. D. Kruijssen et al. 2014). Another hypothesis suggests that star formation in the CMZ occurs episodically and is currently in an inactive phase (J. M. D. Kruijssen et al. 2014; M. R. Krumholz & J. M. D. Kruijssen 2015). However, the strong magnetic field in the CMZ can also delay the collapse of molecular clouds, thereby suppressing star formation. For example, T. Pillai et al. (2015) found that G0.253+0.016 is strongly magnetized, with the magnetic field dominating over turbulence and gravity. The cloud exhibits only a single site of star formation (J. Kauffmann et al. 2013; X. Lu et al. 2019b; D. L. Walker et al. 2021). In contrast, the ministarburst region Sgr B2 (SFR $\sim 0.01\,M_\odot\,\mathrm{yr^{-1}}$; J. Kauffmann et al. 2017; A. Ginsburg et al. 2018) exhibits a relatively weak magnetic field compared to its gravitational and turbulent kinetic energies (X. Pan et al. 2024). Therefore, it is necessary to take magnetic field into account to investigate the low star formation efficiency in the CMZ. Nevertheless, our understanding of magnetic fields in the CMZ remains incomplete, largely due to the limited number of detailed observations.

Recent advances have been made through several large-scale infrared and millimeter surveys targeting the magnetic fields in this region. For example, the PILOT survey (2.′2 resolution, at 240 μm from A. Mangilli et al. 2019) and the Atacama Cosmology Telescope observations (∼1′ resolution, at 98, 150, and 224 GHz from Y. Guan et al. 2021) have uncovered large-scale magnetic fields (≳10 pc) that are both ordered and tilted relative to the Galactic plane. Additionally, higher-resolution surveys such as the Far-Infrared Polarimetric Large-Area CMZ Exploration (FIREPLACE; 19.″6 at 214 μm; N. O. Butterfield et al. 2024; D. Paré et al. 2024), James Clerk Maxwell Telescope (JCMT)/POL2 observations of 11 CMZ molecular clouds from X. Lu et al. (2024), and the B-fields In STar-forming Region Observations (BISTRO, 12″ at 850 μm J. Karoly et al. 2025; M.-Z. Yang et al. 2025) have revealed diverse magnetic field morphologies within individual molecular clouds. Additionally, Y. Hu et al. (2022) used the Gradient Technique and revealed that the magnetic field in the CMZ is globally consistent with the polarization measurements, indicating that the magnetic field and turbulence are dynamically important in the CMZ. These data sets provide an unprecedented opportunity to investigate the role of magnetic fields in the dynamics and star formation processes of CMZ clouds.

The role of magnetic fields in star formation is often assessed by measuring their strength using the Zeeman effect or the Davis–Chandrasekhar–Fermi (DCF) method (L. Davis 1951; S. Chandrasekhar & E. Fermi 1953) and comparing the associated magnetic energy to the turbulent kinetic and gravitational energies. Alternatively, magnetohydrodynamic (MHD) simulations (J. D. Soler et al. 2013; J. D. Soler & P. Hennebelle 2017) have introduced the Histogram of Relative Orientations (HRO), a statistical method to assess the role of magnetic fields. This statistical approach characterizes the relative orientation between the magnetic field and column density structures to infer the energy balance between the magnetic field, gravity, and turbulence. Observational studies (e.g., Planck Collaboration et al. 2016b; J. D. Soler et al. 2017; L. M. Fissel et al. 2019; J. D. Soler 2019) have applied the HRO analysis to Galactic molecular clouds. These studies reveal a clear trend: as column density increases, the relative orientation between magnetic fields and density structures transitions from predominantly parallel in diffuse regions to perpendicular in denser regions. Areas where the magnetic fields are orthogonal to the density structures are typically gravitationally unstable, facilitating star formation. This behavior is consistent with predictions from MHD simulations with initial conditions of sub- to trans-Alfvénic turbulence.

Using the HRO analysis, D. M. Paré et al. (2025) found that magnetic fields in the CMZ are generally aligned parallel to column density structures in dense regions, which is different from that observed in the Galactic disk. However, Planck Collaboration et al. (2016b) have shown that such parallel alignments in 2D projection do not necessarily imply a true 3D parallel configuration. The underlying distribution may still include structures with nearly perpendicular orientations. This highlights the need to test whether the observed preferentially parallel alignments in the CMZ are intrinsic or merely a result of projection effects. Moreover, MHD simulations of the Galactic disk have shown that a transition from parallel to perpendicular relative orientations is linked to the balance between magnetic, turbulent kinetic, and gravitational

energies. Understanding the energy balance in the CMZ may therefore provide insight into the origin of the observed preferential alignment.

In this paper, we investigate the evolution of the relative orientation between magnetic fields and column density structures by applying the HRO analysis with a normalized parameter. To better resolve the relative orientation in dense regions, we increase the number of column density bins at high densities. We also derive a high angular resolution (∼19″) column density map using spectral energy distribution (SED) fitting that combines Herschel and ATLASGAL data. Furthermore, we examine the impact of projection effects using MHD simulations specified to the CMZ environment and explore how energy balance influences the observed magnetic field–density alignment in this unique region. The paper is organized as follows: Section 2 introduces the data used in our analysis. Section 3 presents the results of the relative orientation analysis for the entire CMZ and individual clouds within. We also compare these observational results with state-of-the-art MHD simulations to investigate the effects of line-of-sight (LOS) projection. In Section 4, we explore the energy balance between magnetic, turbulent kinetic, and gravitational energy, as well as the possible origin of the observed relative orientation trends. Finally, Section 5 summarizes the key findings of this study.

2. Observations

2.1. SOFIA Observations

We present the SOFIA (D. A. Harper et al. 2018; P. Temi et al. 2018) 214 μm polarization data from the FIREPLACE survey. The survey covered the entire CMZ, spanning from Sgr B2 to Sgr C (a roughly 1.°5 × 0.°5 region), and achieved an angular resolution of 19.″6. The resulting pixel size is 4.″55. We refer readers to N. O. Butterfield et al. (2024) and D. Paré et al. (2024) for an overview and observation details for the entire survey. These studies also demonstrate that the magnetic fields observed by FIREPLACE generally follow the morphologies of individual clouds, suggesting that the observed fields are predominantly local to the CMZ rather than arising from unrelated LOS components.

2.2. Column Density Map

The column density distribution in the CMZ is derived by fitting a modified blackbody model to the dust SED. To construct the dust SED, we used the Herschel data at 160, 250, 350, and 500 μm from the Hi-GAL survey (S. Molinari et al. 2010) and 870 μm dust emission obtained from the combination of APEX/LABOCA data from the APEX Telescope Large Area Survey of the Galaxy (ATLASGAL; F. Schuller et al. 2009; T. Csengeri et al. 2014) and Planck/high frequency instrument (Planck Collaboration et al. 2014). The ATLAS-GAL data did not account for line contamination. However, as discussed in F. Schuller et al. (2009), the impact of line contamination is generally within the 15% flux calibration uncertainty, except in extreme cases such as hot molecular cores, strong outflow sources, and bright photon-dominated regions. Thus, it is unlikely to significantly affect the majority of the CMZ. Assuming a single-temperature modified blackbody model, the intensity at each wavelength is given by

$$I(\nu) = (1 - e^{-\tau_\nu})B_\nu(T_d), \qquad (1)$$

where $B_\nu(T_d)$ is the Planck function at dust temperature T_d and τ_ν is the optical depth at frequency ν, expressed as

$$\tau_\nu = \frac{\kappa_0 \mu m_H N_{H_2}}{g}\left(\frac{\nu}{\nu_0}\right)^\beta, \tag{2}$$

where κ_0 is the dust opacity per unit mass at frequency ν_0, $\mu = 2.8$ is the mean molecular weight, m_H is the mass of atomic hydrogen, β is the dust emissivity index, and $g = 100$ is the gas-to-dust ratio. We adopt $\kappa_0 = 1.37\,\mathrm{cm}^2\,\mathrm{g}^{-1}$ at $\nu_0 = 300\,\mathrm{GHz}$ from V. Ossenkopf & T. Henning (1994) for coagulated dust grains with thin ice mantles. However, it is important to note that fitting a single-temperature model can bias the temperature estimate toward higher values, particularly when short-wavelength data are missing. In such cases, warmer dust tends to dominate the SED, as it emits more strongly in the far-infrared.

Using the SED fitting method described in Y. Tang et al. (2021), we derive the distributions of column density (N_{H_2}), dust temperature (T_d), and dust emissivity index (β) across the CMZ. The resolution of the resulting column density map is primarily set by the longest-wavelength data from ATLAS-GAL, approximately $19''$ (F. Schuller et al. 2009), which is comparable to the resolution of the SOFIA data. The column density map is sampled at $4''.55$ pixel^{-1}, consistent with the FIREPLACE data, which allows us to make direct comparisons between magnetic fields and column density structures. Figure 1 shows the distribution of column densities and dust temperature in the CMZ overlaid with magnetic field orientations from SOFIA data. Due to saturation in the Herschel data at $160\,\mu m$ in the dense regions of Sgr B2, we masked out the saturated regions in the column density map. The distribution of column densities in the CMZ is similar to the previous work that derived the column density using different methods (e.g., S. Molinari et al. 2011; E. A. C. Mills & C. Battersby 2017; C. Battersby et al. 2024; D. M. Paré et al. 2025). We found pixels with unusually high temperatures ($\gtrsim 50\,K$) but large uncertainties ($\sigma_T > 6\,K$; see Appendix A, Figure 8). We attribute this to overfitting, likely due to the absence of short-wavelength data (e.g., $<100\,\mu m$), which are essential for accurately constraining high-temperature regions ($>30\,K$). Therefore, we masked out the regions with large temperature uncertainties ($\sigma_T \geqslant 6\,K$) in the following analysis.

3. Relative Orientation Analysis

Here we use the HRO method proposed by J. D. Soler et al. (2013) to quantitatively analyze the relative orientation between the column density structures of the CMZ and the magnetic fields revealed by SOFIA. In this method, the column density structures are characterized by their gradient, which is perpendicular to the isodensity contours. We define the relative angle following J. D. Soler et al. (2017):

$$\phi = \tan^{-1}(|\nabla N_{H_2} \times \hat{E}|, \nabla N_{H_2} \cdot \hat{E}), \tag{3}$$

where ∇N_{H_2} is the local gradient of the column density map and $\hat{E}$ is the unit polarization pseudovector, which is perpendicular to the magnetic field. The column density map, derived from SED fitting of Herschel and ATLASGAL data, has a resolution of about $19''$, matching that of the SOFIA observations. This consistency allows for a direct comparison

between the magnetic field orientation and the column density gradient (∇N_{H_2}). Meanwhile, the corresponding spatial resolution of the column density map is about $0.7\,pc$ at a distance of $8.1\,kpc$. Therefore, our HRO analysis here focuses on the cloud scale, comparable to the scale investigated in MHD simulations (J. D. Soler et al. 2013) and archival observations (e.g., Planck Collaboration et al. 2016b; J. D. Soler et al. 2017).

To normalize the relative orientation, we use the normalized alignment measure (AM) parameter introduced in A. Lazarian & K. H. Yuen (2018):

$$\mathrm{AM} = \langle\cos 2\phi\rangle. \tag{4}$$

The uncertainty of AM is given by J. Liu et al. (2023; see their Appendix B):

$$\delta\mathrm{AM} = \sqrt{(\langle(\cos 2\phi)^2\rangle - \mathrm{AM}^2 + \sum(2\sin(2\phi)\delta\phi)^2)/n'}, \tag{5}$$

where n' is the number of independent data points within each density bin. In our study, $\mathrm{AM} > 0$ indicates that the magnetic field is preferentially parallel to the density structure, $\mathrm{AM} < 0$ indicates that the magnetic field is preferentially perpendicular to the density structure, and $\mathrm{AM} \sim 0$ indicates no preferred relative orientation between magnetic field and density structure.

3.1. Relative Orientations in the Entire CMZ

Following N. O. Butterfield et al. (2024) and D. Paré et al. (2024), we apply cuts in the Stokes I intensity threshold of $I/\sigma_I > 200$, percentage polarization less than 50%, and polarization intensity threshold of $P/\sigma_P > 3$, to derive the magnetic field orientation. For the column density map, we apply a cut of $N_{H_2} = 2.0 \times 10^{22}$ cm^{-2}, as indicated by the black contour in Figure 1, which roughly corresponds to the 200σ limit of the Stokes I emission in the SOFIA data. Then, we calculate AM over a set of relative angles within different column density bins.

Figure 2 shows the relative orientation between the magnetic field and density structures as a function of column densities. Following Planck Collaboration et al. (2016b), we use an equal number of data points in each bin to ensure comparable statistics across density bins. The number of data points in each N_{H_2} bin is selected to provide a sufficient number of independent measures per bin for reliable statistical analysis, while also maintaining enough N_{H_2} bins to adequately resolve high-density regions. Therefore, we use 1800 pixels (~ 100 independent polarization measurements) per bin for the entire CMZ. We confirm that varying the number of independent measurements in each column density bin by a factor of two does not significantly affect the observed trend in the relative orientation–column density relation. While the relative orientations between column density structures and magnetic fields appear random in low-density regions ($2 \times 10^{22} < N_{H_2} < 10^{23}$ cm^{-2}), they become more parallel in high-density regions ($N_{H_2} \gtrsim 10^{23}$ cm^{-2}). D. M. Paré et al. (2025) also find a strong preference for parallel orientations to column density structures. This contrasts with previous HRO studies of Galactic disk molecular clouds (e.g., J. Malinen et al. 2016; Planck Collaboration et al. 2016b; J. D. Soler et al. 2017; M. C.-Y. Chen et al. 2024), which consistently observe a
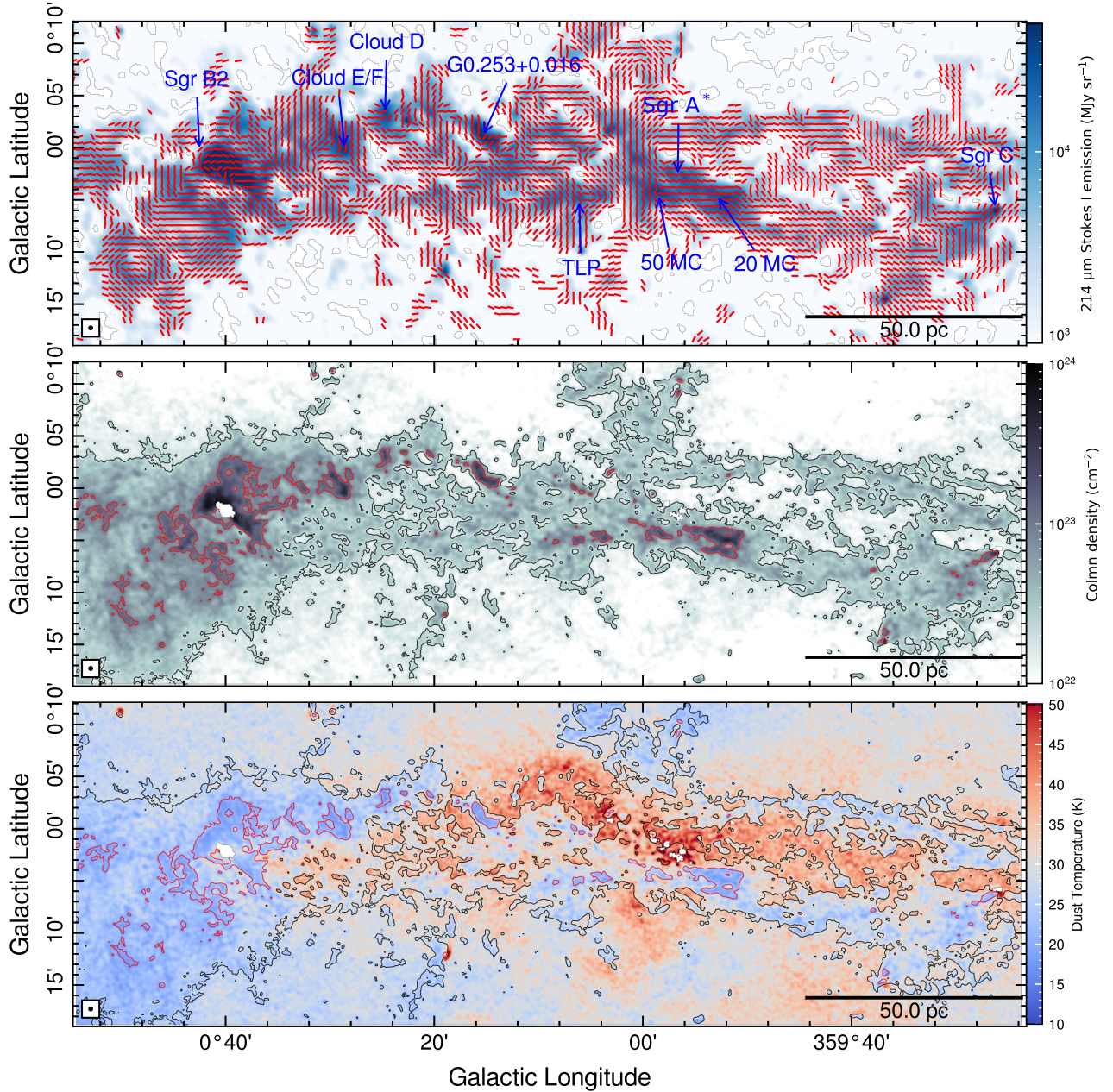
Figure 1. Column density and dust temperature map of the CMZ derived via SED fitting. The top panel shows 214 μm SOFIA/HAWC+ Stokes I emission overlaid with magnetic field orientations. Red segments indicate the plane-of-sky magnetic field orientations, and labeled blue arrows highlight prominent CMZ molecular clouds. The middle panel shows the distribution of column densities derived by fitting a modified blackbody function to the 160, 250, 350, and 500 μm Herschel data from S. Molinari et al. (2010) and 870 μm dust emission obtained from the combination of Planck and APEX data from T. Csengeri et al. (2014). Column density values corresponding to dust temperature uncertainties over 6 K have been masked. The black contour marks a column density of $N_{H_2} = 2 \times 10^{22}$ cm^{-2}. The red contour marks a column density of $N_{H_2} = 10^{23}$ cm^{-2}, where the relative orientation between magnetic fields and column density structures for the CMZ becomes more parallel. The bottom panel shows the distribution of dust temperatures.

transition from parallel to perpendicular alignment with increasing density. However, in those cases, the transition occurs at significantly lower densities (10^{21}–10^{22} cm^{-2}) than the average density in the CMZ.

3.2. Relative Orientations in Individual Molecular Clouds in the CMZ

The CMZ contains several molecular clouds like Sgr B2, Sgr C, the 20 km s^{-1} cloud (hereafter referred to as 20MC), the 50 km s^{-1} cloud (hereafter referred to as 50MC), G0.253 +0.016 (the Brick), and the Dust Ridge clouds, showing different levels of star formation activity. Some of these clouds, like Sgr C and 50MC, have higher SFRs ($\sim 10^{-2} M_{\odot}$ yr^{-1}), in agreement with the empirical relation between the star formation and the amount of the dense gas (A. T. Barnes et al. 2017; J. Kauffmann et al. 2017; D. L. Walker et al. 2018; X. Lu et al. 2019b). With its high SFR and efficiency, Sgr B2 hosts one of the rare ministarburst regions in our Galaxy (R. A. Gaume et al. 1995; S. L. Qin et al. 2011; A. Ginsburg et al. 2018; X. Pan et al. 2024). In contrast, other clouds such as G0.253+0.016 are more quiescent (X. Lu et al. 2015; D. L. Walker et al. 2021). In Figure 3, we present the distribution of relative orientations in
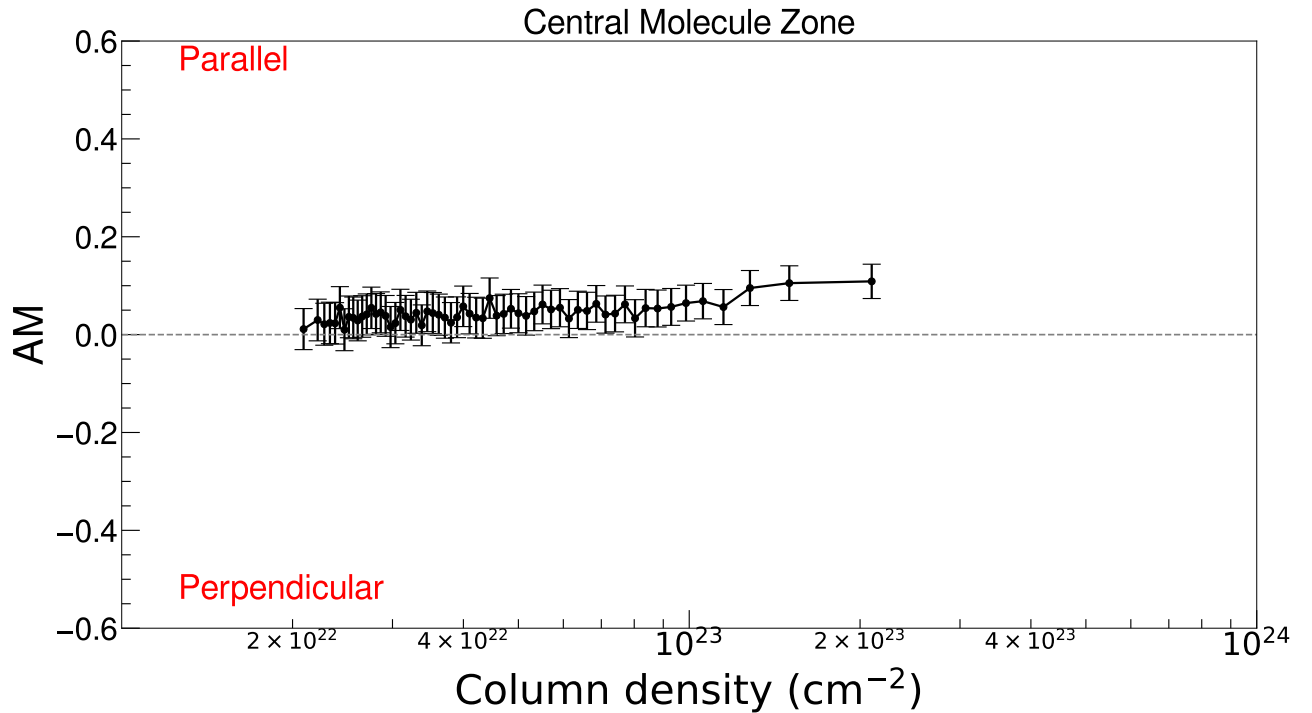
Figure 2. Relative orientation between magnetic field and column density structure as a function of column density for the entire CMZ, characterized by AM. AM > 0 corresponds to magnetic field preferentially parallel to the column density structure, while AM < 0 corresponds to magnetic field preferentially perpendicular to the column density structure. AM ∼ 0 indicates that the relative orientation between magnetic field and column density structure is random.

these molecular clouds, with each density bin containing 180 pixels (∼10 independent polarization measurements). We also verify that changing the number of independent measurements in each density bin by a factor of two does not significantly alter the trend on the relative orientation–column density relations. However, increasing the number of measurements per bin can smooth out alignment transitions, particularly in high-density bins where a parallel-to-perpendicular shift occurs. To preserve these alignment changes, we adopt 10 independent measurements per density bin. We use an intensity threshold of $108\,\mathrm{Jy\,beam^{-1}}$ (corresponding to a column density of $4 \times 10^{22}\,\mathrm{cm^{-2}}$ with a dust temperature of 30 K) on 214 μm SOFIA/HAWC+ Stokes I emission to define the coverage of individual molecular clouds, expect for Sgr B2, as indicated by the black contour in Figures 4 and 5. The cyan segments show the orientations of density gradients in each molecular cloud. For Sgr B2, considering its high brightness, we applied a higher threshold of $145\,\mathrm{Jy\,beam^{-1}}$ (corresponding to a column density of $6 \times 10^{22}\,\mathrm{cm^{-2}}$ with a dust temperature of 30 K).

Some molecular clouds, such as Dust Ridge Clouds B and C, are relatively small and lack sufficient independent polarization detections ($\lesssim$12) to reliably trace magnetic field alignments across different density bins. As a result, we exclude these clouds from our analysis. Future higher-resolution observations will be necessary to study their magnetic field–column density relationships in detail. 20MC and 50MC, on the other hand, are close to each other in the plane of the sky and are both exceptionally bright, making it impossible to spatially distinguish them using a continuum intensity threshold of $108\,\mathrm{Jy\,beam^{-1}}$. Instead, we separated them using kinematic information. The systematic velocities for 20MC and 50MC are 20 and $50\,\mathrm{km\,s^{-1}}$, respectively. Based on J. D. Henshaw et al. (2016), both clouds have

velocity dispersions around $9\,\mathrm{km\,s^{-1}}$, corresponding to a line full width at half-maximum of about $21\,\mathrm{km\,s^{-1}}$. We integrated the HNCO $(4_{0,4}–3_{0,3})$ data from the Mopra CMZ survey (P. A. Jones et al. 2012) over the velocity ranges of $6–26\,\mathrm{km\,s^{-1}}$ for 20MC and $38–58\,\mathrm{km\,s^{-1}}$ for 50MC, excluding the overlapping regions. The blue contours in Figure 4 show the coverage of 20MC and 50MC. The "Three Little Pigs" (TLP; C. Battersby et al. 2020) cloud complex consists of M0.145-0.086 (Straw), M0.106-0.082 (Sticks), and M0.068-0.075 (Stone). The spatial and kinematic separations between each other are relatively small, suggesting that they are likely associated. Therefore, we analyze TLP as a single cloud to study the relative orientation between the magnetic field and the column density structure.

We find various alignment behaviors in different molecular clouds. In 20MC, 50MC, and G0.253+0.016, almost all density bins exhibit positive AM values, indicating a preferential parallel alignment between the magnetic field and the density structure in these regions.

Sgr B2 also shows positive AM values across most column density bins and a decreasing trend with increasing column density. However, some intermediate-density bins exhibit AM values close to zero, suggesting a lack of preferential alignment between the magnetic field and column density structures in those regions. In particular, the two massive dense cores (North and Main) in Sgr B2 are saturated in the Herschel 160 μm data, resulting in blank regions in the column density map. Previous studies (D. C. Lis & P. F. Goldsmith 1991; S. Huttemeister et al. 1993; X. Pan et al. 2024) have shown that these regions have extremely high column densities, exceeding $10^{24}\,\mathrm{cm^{-2}}$, leaving us with no information on the relative orientation of the magnetic field in the densest regions of Sgr B2.
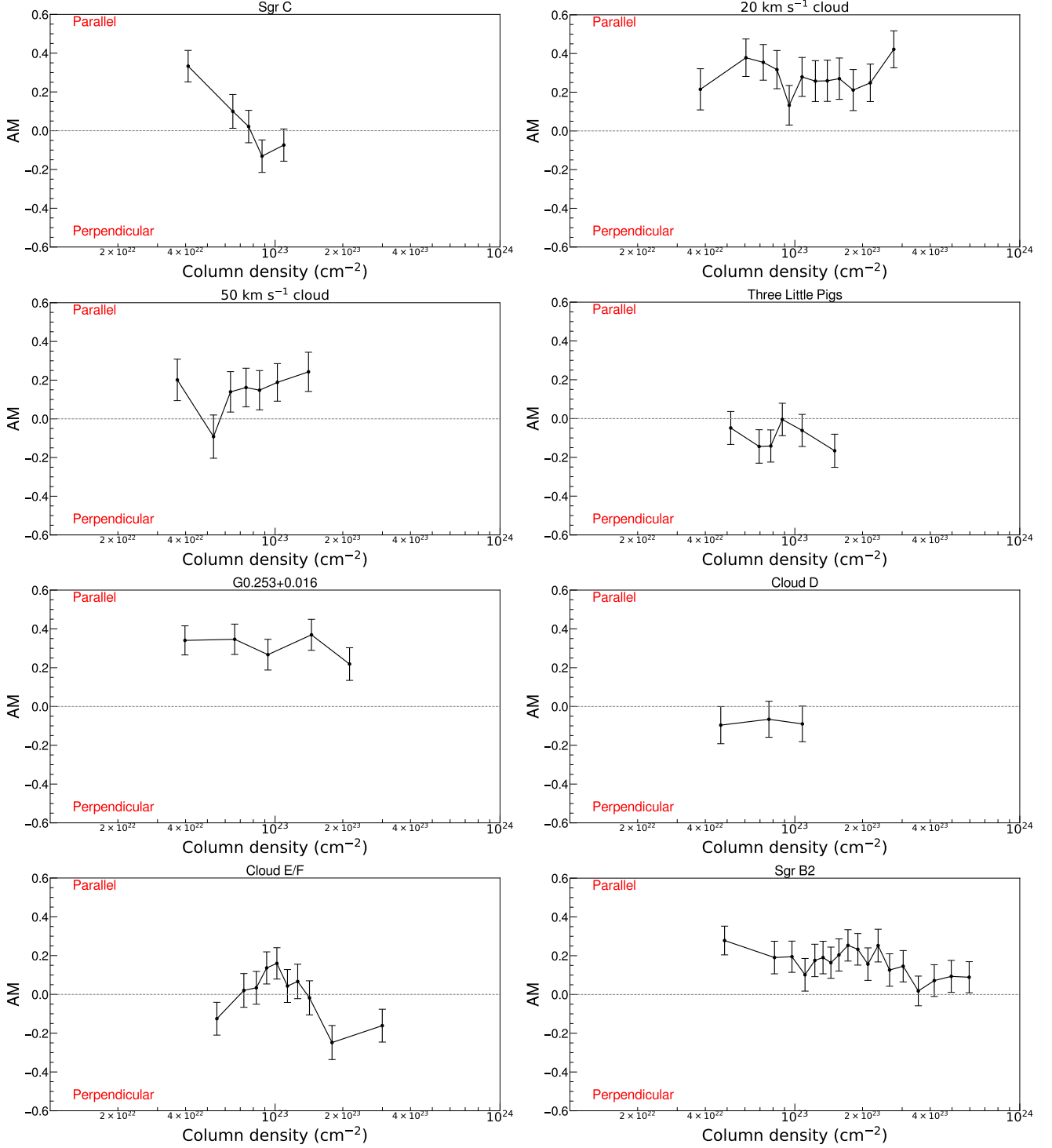
Figure 3. Relative orientation between magnetic field and column density structure as a function of column density for the individual clouds in the CMZ, characterized by AM. AM > 0 corresponds to magnetic field preferentially parallel to the column density structure, while AM < 0 corresponds to magnetic field preferentially perpendicular to the column density structure. AM ∼ 0 indicates that the relative orientation between magnetic field and column density structure is random.

To address this, we derive the column density (N_{H_2}) map for the densest regions using 214 μm continuum emission, assuming optically thin dust emission. The column density is calculated as

$$N_{H_2} = \frac{g S_\nu D^2}{\mu m_H B_\nu(T_d) \kappa_\nu A},$$ (6)

where $g = 100$ is the gas-to-dust ratio, S_ν is the flux per pixel, $D = 8.3$ kpc is the distance, $\mu = 2.8$ is the mean molecular

weight, $B_\nu(T_d)$ is the Planck function at the dust temperature T_d, κ_ν is the dust opacity, and A is the physical area of each pixel. The dust opacity is assumed to follow $\kappa_\nu = \kappa_0(\nu/300\,\text{GHz})^\beta$, consistent with the approach used in our SED fitting. We adopt a dust emissivity index $\beta = 2.0$, similar to the mean values observed in other dense molecular clouds such as Sgr C ($\bar{\beta} = 2.2$) and G0.253+0.16 ($\bar{\beta} = 1.9$). The dust temperature is fixed at 20 K for Sgr B2, as suggested by
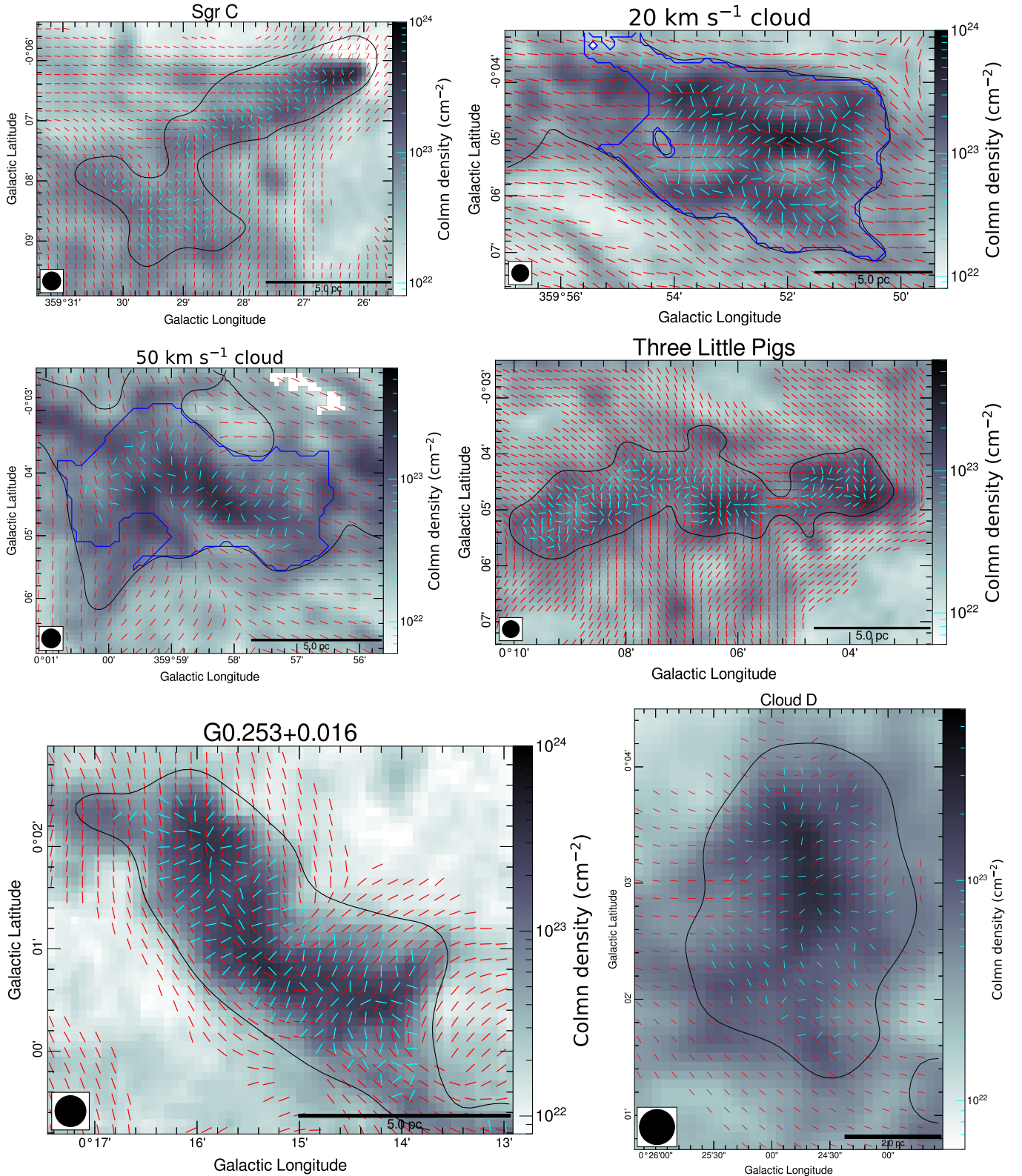
Figure 4. Comparisons between orientations of magnetic fields and column density structures for individual molecular clouds. Red and cyan segments represent plane-of-sky magnetic field orientations and column density gradient orientations, respectively. The black contour marks an intensity threshold of 108 Jy beam^{-1} for 214 μm SOFIA/HAWC+ Stokes I emission, indicating the region used for HRO analysis. Blue contours in 20MC and 50MC highlight regions used for HRO analysis that are separated by kinematics.

D. Pierce-Price et al. (2000) and M. Etxaluze et al. (2013). Appendix B, Figure 9 shows the derived column density map of Sgr B2, covering the densest regions. We find great

consistency between the column densities obtained from SED fitting and those derived using the single-wavelength method. Appendix B, Figure 9 also shows the HRO results for a newly
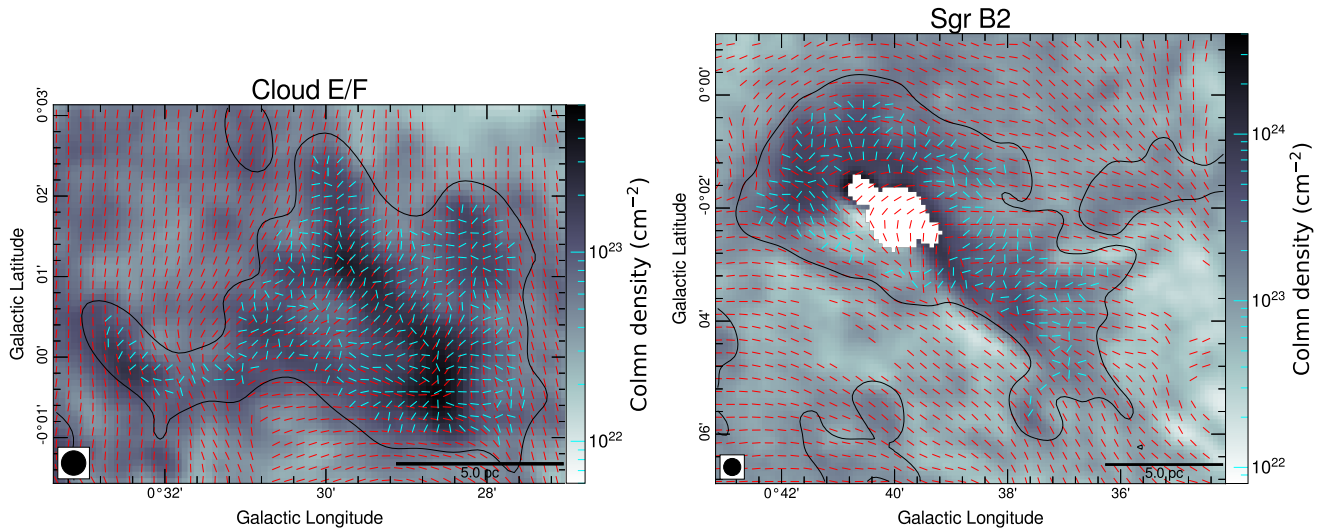
Figure 5. Comparison between the orientations of magnetic field and column density structure for Cloud E/F and Sgr B2. The panel format is the same as for Figure 4. For Sgr B2, the black contour marks an intensity threshold of 145 Jy beam^{-1} for 214 μm SOFIA/HAWC+ Stokes I emission.

derived column density map; we find that the relative orientations between magnetic field and column density in Sgr B2 transit from parallel to perpendicular at regions with highest density ($N_{\mathrm{H_2}} \gtrsim 8 \times 10^{23}$ cm^{-2}).

Sgr C shows positive AM values in low-density regimes and a decrease to the negative AM values as density increases, similar to what we observed in star-forming regions in the Galactic disk (e.g., Planck Collaboration et al. 2016b; J. D. Soler et al. 2017). However, the critical density (N_{crit}) where the transition happens is around 8×10^{22} cm^{-2}, which is much higher than the typical value ($\sim 10^{21}$–10^{22} cm^{-2}) in the Galactic disk. Dust Ridge Cloud E/F (also known as Sgr B1 off) presents a more complex situation. The relative orientations between magnetic fields and column density structures shift from perpendicular to parallel and back to perpendicular as density increases. In the TLP region, most density bins exhibit negative AM values, indicating a preferential perpendicular alignment between the magnetic field and the density structures. However, some intermediate-density bins have AM values close to zero, suggesting more complex or random relative orientations in those regions. In Dust Ridge Cloud D, all three density bins also show negative AM values, but their magnitudes are close to zero. This suggests that the magnetic field in this cloud may not exhibit a clear preferential orientation relative to the column density structures. Given that this region is not well resolved, higher-resolution observations are needed to more accurately determine the underlying alignment patterns. The relative alignments for each molecular cloud in the CMZ are summarized in Table 1.

D. M. Paré et al. (2025) also examined the relative orientation between magnetic fields and column density structures in individual molecular clouds, categorizing the clouds into three density bins (low, intermediate, and high) for their analysis. While most clouds (e.g., 20MC, TLP, G0.253 +0.016) exhibited trends consistent with our findings, we find a difference in Sgr C and Cloud E/F when increasing the number of column density bins to better resolve high-density regions. Unlike the parallel alignment reported by D. M. Paré et al. (2025) across low-, intermediate-, and high-density bins, we find a transition from parallel to perpendicular relative

orientations at the highest densities in these clouds. This is possibly due to more bins for high-density regions in our analysis that are able to reveal more details of relative orientations in dense regions. In fact, the HRO plots for Sgr C and Cloud E/F in D. M. Paré et al. (2025; see their Figures 7 and 9) both showed a bimodal distribution of relative orientation in the high-density bins, with one peak perpendicular and the other parallel.

3.3. Comparison with MHD Simulations of CMZ

Numerical simulations (e.g., J. D. Soler et al. 2013; D. Seifried et al. 2020; P. Girichidis 2021) demonstrate that projection effects can significantly impact 2D relative orientation analyses. For example, a parallel or random alignment observed in 2D (AM > 0) does not necessarily rule out a perpendicular alignment in 3D (AM < 0) between magnetic fields and dense structures (see Appendix C in Planck Collaboration et al. 2016b). To check whether the preferential parallel alignment observed in the CMZ is genuine, we examined a 3D MHD simulation that approximates CMZ-like conditions (R. Tress et al. 2025, in preparation).

The simulations are designed to study gas dynamics and star formation in the CMZ in the presence of magnetic fields and stellar feedback. They build on those presented in R. G. Tress et al. (2020, 2024), using the same initial conditions but incorporating additional physical processes and higher resolution. They are performed using the moving-mesh code AREPO (V. Springel 2010; R. Weinberger et al. 2020) and include an external barred potential fine-tuned to the Milky Way (G. H. Hunter et al. 2024), a time-dependent chemical network that keeps track of hydrogen and carbon chemistry (S. C. O. Glover & P. C. Clark 2012), a physically motivated model for the formation of new stars using star particles, supernova feedback and ionizing radiation feedback from massive stars through the SWEEP method for "on-the-fly" radiative transfer (T. Peter et al. 2023), and magnetic fields through the ideal MHD scheme implemented in AREPO (R. Pakmor et al. 2011; R. Pakmor & V. Springel 2013). The simulations follow the interstellar medium (ISM) evolution in the entire barred region of the simulated Milky Way and are therefore able to self-consistently follow the formation of

<div align="center">

Table 1
Physical Properties of the Individual Molecular Clouds

</div>

Source	Mass[a] $(10^4\,M_\odot)$	$R_{\rm eff}$[b] (pc)	$n({\rm H_2})$ $(10^3\,{\rm cm}^{-3})$	$\sigma_{\rm turb}$ $({\rm km\,s}^{-1})$	$B_{\rm pos}$[c] (mG)	λ	$\mathcal{M}_A$	α_{k+B}[d]	RO Evolution[e]
Sgr C	6.7	3.3	6.1	6.9	0.28	1.8	2.0	1.8–2.9	$\parallel$ to $\perp$/R
20 km s^{-1}	23.4	4.9	6.8	7.7	0.55	1.5	1.3	1.2–1.9	$\parallel$
50 km s^{-1}	8.4	3.7	5.4	10.2	0.98	0.5	0.8	3.8–6.0	$\parallel$/R to $\parallel$
TLP	9.1	3.8	5.6	8.9	0.28	1.9	2.5	2.4–4.0	$\perp$/R to $\perp$
G0.253+0.016	9.7	3.3	9.2	14.8	1.17	0.6	1.3	5.5–9.0	$\parallel$
Cloud D	3.8	2.5	8.6	10.0	0.64	0.8	1.5	4.7–7.7	R
Cloud E/F	19.4	4.7	6.2	10.8	0.71	1.0	1.3	2.3–3.6	$\perp$ to $\parallel$/R to $\perp$
Sgr B2[f]	325.0	6.1	48.1	9.3	0.45	20.3	6.1	0.1–0.2	$\parallel$ to $\perp$[g]

Notes.
[a] Gas mass for individual molecular clouds derived from the column density map.
[b] Effective radius for the molecular cloud.
[c] The total plane-of-sky magnetic field strength estimated by the ADF method.
[d] The virial parameter calculated for density profiles with power-law index β ($\rho \propto r^{-\beta}$), where β ranges from 0 to 2.
[e] The evolution of the relative orientation between the magnetic field and the column density structures within each cloud as a function of increasing column density.
"$\parallel$" means preferential parallel orientation. "$\perp$" means preferential perpendicular orientation. "R" means no preferential orientation.
[f] The properties of Sgr B2 are from X. Pan et al. (2024) since the dense regions in Sgr B2 are masked out in the column density map.
[g] Sgr B2 shows a transition from parallel to perpendicular when we include the highest-density regions, which are saturated in 160 μm Herschel data.
[h] SFR for each molecular cloud referred from H. P. Hatchfield et al. (2024). The SFR of Sgr B2 is from A. Ginsburg et al. (2018).

magnetized molecular clouds and their embedded star formation from the large-scale flow. The adopted mass resolution is $20\,M_\odot$, which corresponds to spatial resolution <1 pc for ISM densities above $10^2\,{\rm cm}^{-3}$.

To compare MHD simulations with observations, we used the radiative transfer code POLArized RadIation Simulator (POLARIS; S. Reissl et al. 2016) to create synthetic dust polarization maps of the CMZ, assuming radiative torque alignment to be the primary dust grain alignment mechanism in the CMZ as suggested in N. O. Butterfield et al. (2024). The simulations produced by the AREPO code use unstructured grids with cell sizes that vary spatially. Because the coarsest resolution in the diffuse regions of the simulations is comparable to that of the observational data, we employ POLARIS to project the simulation onto a uniform grid with a spatial resolution of 0.6 pc, which matches the resolution of our observational data. Meanwhile, the AREPO MHD simulations provided the coordinates and masses of heating sources, and we derived the surface temperatures required for POLARIS inputs using the empirical mass–luminosity relation $L_* \propto M_*^{3.5}$ (G. P. Kuiper 1938) and mass–radius relation $R_* \propto M_*^{0.8}$ (O. Demircan & G. Kahraman 1991). In the synthetic observation, we adopt an external interstellar radiation field typical of the Galactic disk, with a strength of $G_0 = 1$ (J. S. Mathis et al. 1983). The gas-to-dust mass ratio is set to 100, and dust grains are modeled as a mixture of 62.5% astronomical silicates and 37.5% graphite (J. S. Mathis et al. 1977), following a size distribution of $n_d(a) \propto a^{-3.5}$ for grain radii (a) ranging from 0.25 μm to 5 mm. The adopted settings for the interstellar radiation field, gas-to-dust ratio, and dust grain properties are representative of typical Galactic disk conditions, which may differ from those in the Galactic center. In this study, the synthetic observation based on these disklike conditions serves as a simplified test case. Future work will incorporate CMZ-specific properties into the simulations to more accurately reflect the unique physical environment of the CMZ. N. O. Butterfield et al. (2024) and D. Paré et al. (2024) have shown that the FIREPLACE data likely trace the magnetic field local to the CMZ. Therefore, to investigate

the effect of the integration along the LOS on the relative alignment, we only focus on the CMZ region in the simulation.

Figure 6 shows synthetic 214 μm observations of the simulated magnetic field overlaid on a column density map covering the entire CMZ, viewed along three orthogonal planes (x-y, y-z, and x-z) at a distance of 8.1 kpc. Following the HRO analysis above, we derived the column density gradient and applied density masks for different viewing angles. For the edge-on views (x-z and y-z planes), we used a density threshold of $N_{\rm H_2} = 1.0 \times 10^{22}\,{\rm cm}^{-2}$. For the face-on view ($x$-$y$ plane), a lower threshold of $N_{\rm H_2} = 3 \times 10^{21}\,{\rm cm}^{-2}$ was used owing to the reduced LOS material integration. Applying HRO analysis to the synthetic polarization data across these directions (see Figure 7), we found that edge-on views (x-z and y-z planes) show parallel alignment between magnetic fields and column density structures in high-density bins ($N_{\rm H_2} \gtrsim 5 \times 10^{22}\,{\rm cm}^{-2}$) and no preferred alignment in low-density bins, which is consistent with what we observed in SOFIA data, while the face-on view (x-y plane) shows parallel alignment across all density bins.

To connect the alignment in the 2D polarization map with the actual conditions in the MHD simulation, we calculate the relative alignment between the magnetic field and the volume density (n) in 3D. This alignment is quantified by the angle $\psi = \angle(\boldsymbol{B}, n)$, which measures the orientation between the 3D magnetic field and isodensity contours. To maintain consistency with the 2D case, we define ${\rm AM_{3D}} = \langle\cos 2\psi\rangle$, where ${\rm AM_{3D}} > 0$ indicates parallel alignment, ${\rm AM_{3D}} < 0$ indicates perpendicular alignment, and ${\rm AM_{3D}} \sim 0$ indicates no preferred alignment. The bottom right panel of Figure 7 shows positive ${\rm AM_{3D}}$ values across all density bins, indicating that the 3D magnetic fields are generally aligned with the volume density structures. In low-density regions, this alignment is also reflected in the face-on (X-Y plane) 2D projection. However, in the edge-on views (X-Z and Z-Y planes), the projected 2D magnetic fields exhibit no clear preferential alignment at low column densities. A plausible explanation for this discrepancy is the presence of multiple diffuse gas components along the LOS in these edge-on perspectives. This LOS superposition can obscure the underlying 3D alignment, resulting in a
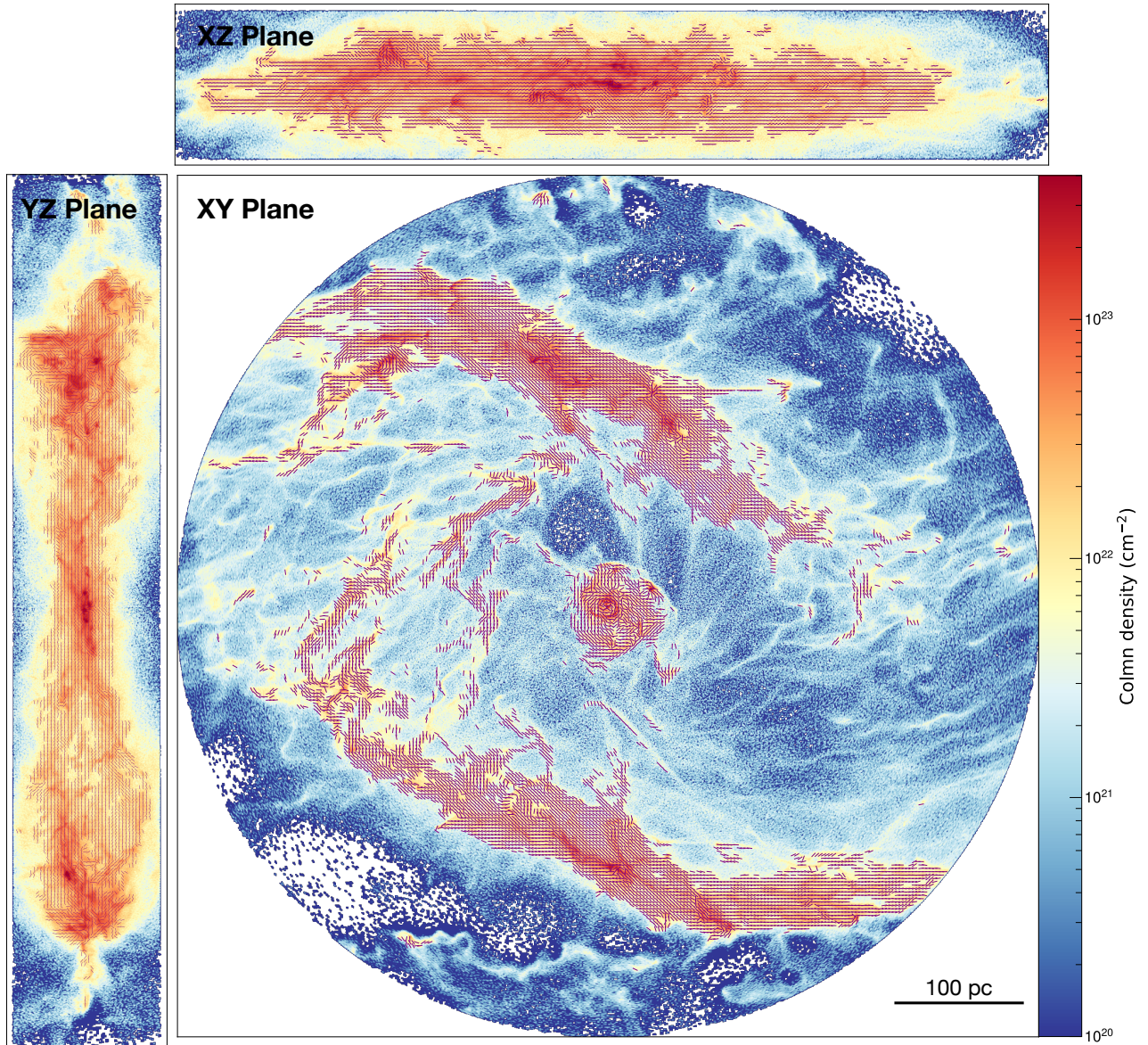
Figure 6. Visualization of the magnetic field and column density in the CMZ for the synthetic observations of the MHD simulation. The color scale represents the gas column density. Purple segments represent the projected magnetic field orientation.

randomization of the projected relative orientation due to averaging over many uncorrelated structures.

In general, we find preferentially parallel alignment in projected 2D and 3D synthetic observations across different densities, suggesting that the observed parallel alignments in SOFIA data are likely to be real instead of caused by a projection effect.

4. Role of Magnetic Fields in CMZ Clouds

Previous studies in the Galactic disk found a general trend in which relative orientations between gas column density structures and magnetic fields transition from parallel at low column densities to preferentially perpendicular at highest column densities (e.g., Planck Collaboration et al. 2016b; J. D. Soler 2019; M. C.-Y. Chen et al. 2024). The transition from parallel to perpendicular alignment usually occurs at $N_{\rm H_2} \sim 10^{21} - 10^{22} {\rm cm}^{-2}$. Numerical simulations (e.g., J. D. Soler et al. 2013; C.-Y. Chen et al. 2016; J. D. Soler et al. 2017; D. Seifried et al. 2020) suggested that the

change in relative orientation may be related to energy balance in the clouds and that the transition occurs in regions in gravitational collapse. Therefore, due to the support provided by strong magnetic field and turbulence in the CMZ, the density where the transition happens in the CMZ may be much higher than that in the Galactic disk. To assess energy balance, we estimate the magnetic field strength and compare its energy with turbulent kinetic and gravitational energy.

4.1. Magnetic Field Strength for Individual Clouds

The DCF method (L. Davis 1951; S. Chandrasekhar & E. Fermi 1953) is widely used to estimate the plane-of-sky magnetic field strength ($B_{\rm pos}$), assuming that magnetic field perturbations are caused by turbulent motion. In this work, we apply a variant of the DCF method, the angular dispersion function (ADF) analysis (D. Falceta-Gonçalves et al. 2008; R. H. Hildebrand et al. 2009; M. Houde et al. 2009, 2016), to quantify variations in magnetic field orientations. For a
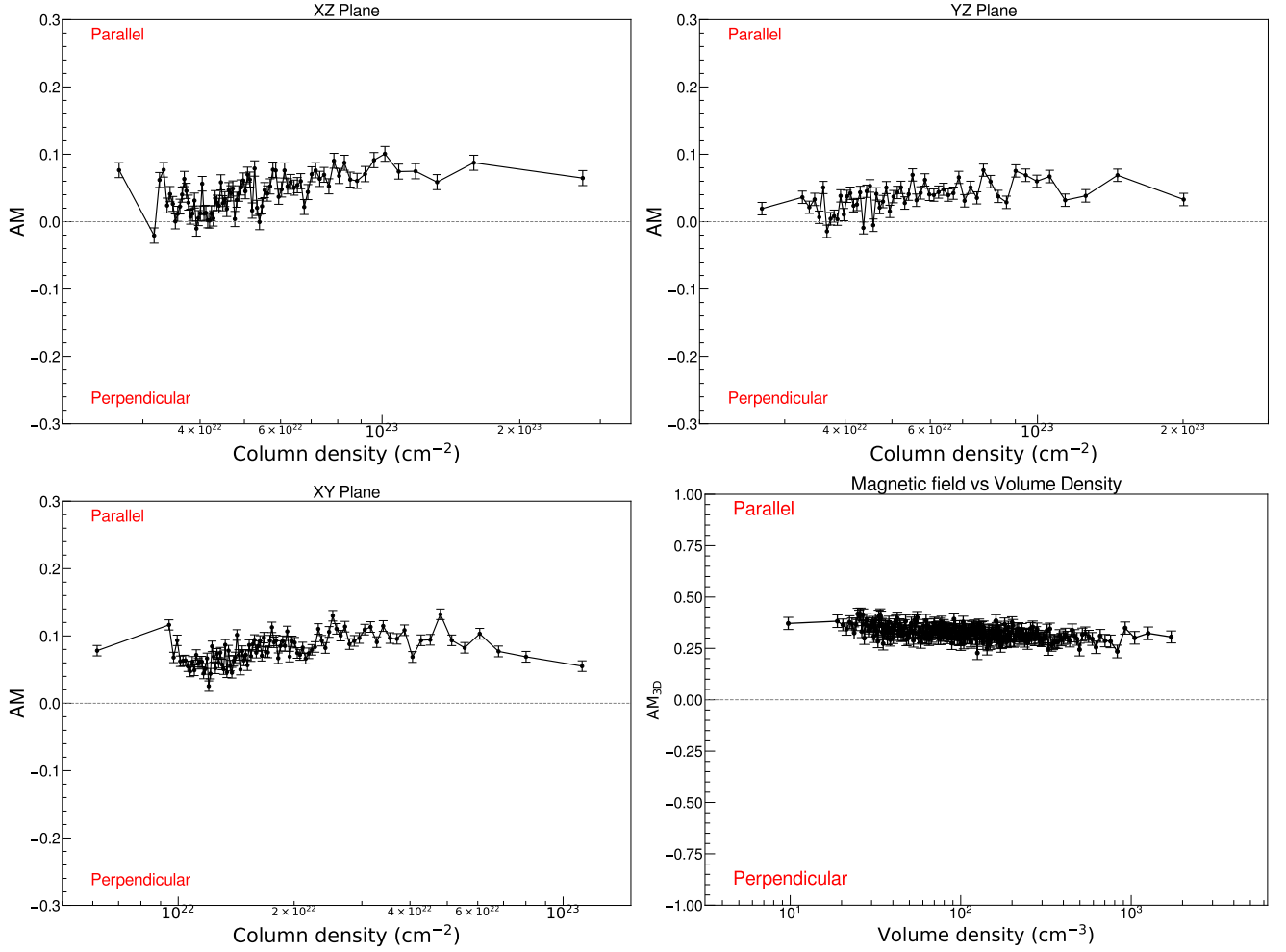
Figure 7. Alignment measures derived from MHD simulations of the CMZ. Top left: projected 2D AM along the *Y*-axis (edge-on view). Top right: projected 2D AM along the *X*-axis (edge-on view). Bottom left: projected 2D AM along the *Z*-axis (face-on view). Bottom right: 3D AMs (AM$_{\text{3D}}$) between magnetic fields and volume density structures across different density bins.

detailed review of the DCF and ADF methods, we refer readers to J. Liu et al. (2022).

Following R. H. Hildebrand et al. (2009), we can obtain the magnetic field strength by

$$B_0 = \sqrt{\mu_0 \rho} \quad \sigma_{\text{turb}} \left[\frac{\langle B_t^2 \rangle}{\langle B_0^2 \rangle} \right]^{-1/2} \tag{7}$$

$$B_{\text{pos}} = Q_c B_0 \sqrt{1 + \left[\frac{\langle B_t^2 \rangle}{\langle B_0^2 \rangle} \right]}, \tag{8}$$

where μ_0 is the vacuum permeability, $\rho = \mu_{\text{H}_2} m_{\text{H}_2} n_{\text{H}_2}$ is the average mass density of gas, σ_{turb} is the turbulent velocity dispersion of the cloud, $(\langle B_t^2 \rangle / \langle B_0^2 \rangle)^{-1/2}$ is the turbulent-to-ordered magnetic field strength ratio, and Q_c is the correction factor. Assuming a spherical geometry for each cloud, we can derive the average volume density (n_{H_2}) of each cloud using an effective radius R_{eff} and gas mass M_{gas} derived from the column density map:

$$n_{\text{H}_2} = 3M_{\text{gas}}/4\mu_{\text{H}_2} m_{\text{H}} \pi R_{\text{eff}}^3. \tag{9}$$

The effective radius of each molecular cloud, $R_{\text{eff}} = \sqrt{A_{\text{cloud}}/\pi}$, is derived from its enclosed area A_{cloud}. $(\langle B_t^2 \rangle / \langle B_0^2 \rangle)^{-1/2}$ can be

derived from the ADF, expressed as (M. Houde et al. 2009, 2016)

$$1 - \langle \cos[\triangle \phi(\ell)] \rangle = \sum_{j=1}^{\infty} a_{2j} \ell^{2j}$$
$$+ \frac{\langle B_t^2 \rangle}{\langle B_0^2 \rangle}[1 - e^{-\ell^2/2(\delta^2 + 2W^2)}], \tag{10}$$

where $\triangle\phi(\ell)$ is the angular dispersion of two polarization segments as a function of distance, ℓ, between them; δ is the turbulence correlation length; and W is the standard deviation of the Gaussian beam. Here we do not apply the LOS signal integration correction proposed by M. Houde et al. (2009) to determine the turbulent-to-ordered magnetic field ratio ($\sqrt{\langle B_t^2 \rangle / \langle B_0^2 \rangle}$). This is because the numerical study by J. Liu et al. (2021) indicates that this correction may not work well within the ADF framework. Instead, to account for the LOS signal integration effect, we adopt the numerically derived correction factor $Q_c = 0.21$ from J. Liu et al. (2021) when we derive the plane-of-sky magnetic field strength. The ADF fitting results of the molecular clouds are shown in Appendix C, Figure 10.

For turbulent velocity dispersion, we used HNCO $(4_{0,4}–3_{0,3})$ data from the Mopra CMZ survey (P. A. Jones et al. 2012). Following Appendix B in X. Pan et al. (2024), we shifted each pixel's spectra to the local intensity-weighted mean velocity and averaged them within the ADF analysis area to separate small-scale turbulence from large-scale bulk motion. A Gaussian function was then fitted to the averaged spectra to determine the velocity dispersion. Given that the dust temperature for most clouds is around 20 K, the thermal motion contribution is negligible. It is worth noting that some regions in the CMZ may exhibit multiple velocity components along the LOS, potentially broadening the averaged line profiles and leading to an overestimation of the velocity dispersion. For example, S. N. Longmore et al. (2012) and D. L. Walker et al. (2015) reported smaller velocity dispersions for G0.253+0.016 and Cloud D using a multi-component Gaussian fitting of the $HN^{13}C$ (10–9) emission from the Mopra CMZ survey (P. A. Jones et al. 2012). However, the majority of the analyzed regions in our work show only a single dominant velocity component, and the derived velocity dispersions are consistent with the intensity-weighted mean values ($\langle\sigma\rangle$) reported by J. D. Henshaw et al. (2016), in which they took multiple LOS components into account. This consistency suggests that our measured dispersions provide reliable estimates of the turbulent motions within these clouds. Appendix D, Figure 11 shows the shifted line spectra. Table 1 lists the estimates of turbulent velocity dispersions.

The uncertainty in the estimated magnetic field strengths is difficult to quantify owing to the inherent limitations of the DCF method. We adopt a typical uncertainty factor of 2, based on J. Liu et al. (2021), who derived this by applying the DCF method to numerical simulations and comparing the estimates to input models. However, this uncertainty should be considered a lower limit, as real-world observations may introduce additional sources of error not accounted for in numerical simulations. The estimated B_{pos} values for the clouds are shown in Table 1. The estimates of magnetic field strength of some molecular clouds (e.g., Sgr C, 50MC, G0.253+0.016, Cloud E/F) from FIREPLACE data are consistent with that from X. Lu et al. (2024) derived by JCMT data at comparable resolution.

4.2. Comparison with Turbulence and Gravity

With the derived magnetic field strength, we can compare the role of magnetic fields with other effects, such as turbulence and gravity.

To quantify the relative significance between magnetic field and turbulence of the individual cloud, we can use Alfvénic Mach number:

$$\mathcal{M}_A = \sigma_{turb,3D}/v_{A,3D}, \tag{11}$$

where $\sigma_{turb,3D} = \sqrt{3}\,\sigma_{turb}$ is an estimate for 3D turbulent velocity dispersion, assuming isotropic turbulence, and $v_{A,3D} = B_{3D}/\sqrt{\mu_0\rho}$ is the 3D Alfvén velocity. The 3D magnetic field strength (B_{3D}) can be estimated from the plane-of-sky field using a statistical relation. Assuming random inclination angles between the 3D and plane-of-sky magnetic fields, R. M. Crutcher et al. (2004) proposed $B_{3D} = 4B_{pos}/\pi$. We found that nearly all molecular clouds

in the CMZ have Alfvénic Mach numbers greater than or approximately equal to 1 ($\mathcal{M}_A \gtrsim 1$), except 50MC. Considering the uncertainties inherent in the DCF method, we conclude that turbulence is likely to play a role as significant as, or possibly more significant than, the magnetic field in most CMZ clouds.

With the estimated magnetic field strengths, we can also assess the balance between magnetic field and gravity in individual clouds by using the mass-to-flux ratio, λ, in units of critical value $1/(2\pi\sqrt{G})$ (T. Nakano & T. Nakamura 1978; R. M. Crutcher et al. 2004):

$$\lambda = \mu_{H_2} m_H \sqrt{\mu_0\pi G}\,\frac{N_{H_2}}{B} \sim 7.6 \times 10^{-21}\frac{N_{H_2}/cm^{-2}}{B_{3D}/\mu G}, \tag{12}$$

where N_{H_2} is the molecular hydrogen column density. In our sample, two clouds (50MC and G0.253+0.016) exhibit relatively low mass-to-flux ratios ($\lambda \sim 0.5$), indicating that magnetic fields may play a dominant role over gravity in these regions. In contrast, the other clouds have mass-to-flux ratios greater than or approximately equal to 1 ($\lambda \gtrsim 1$), suggesting that gravity could be as significant as, or possibly more significant than, the magnetic field in those clouds.

The virial parameter is commonly used to evaluate the stability of a core against gravitational collapse. In the CMZ, where both magnetic fields and turbulence are strong, these forces both provide significant support against collapse (e.g., T. Pillai et al. 2015; P. C. Myers et al. 2022). Following J. Liu et al. (2020), we estimate the virial parameter by incorporating magnetic and kinetic energy:

$$\alpha_{k+B} = \frac{M_{k+B}}{M_{gas}}, \tag{13}$$

where $M_{k+B} = \sqrt{M_B^2 + (M_k/2)^2}$ is the critical virial mass, M_{gas} is the gas mass of the cloud, and β is the power-law index of the cloud's density profile ($\rho \propto r^{-\beta}$). Here M_k and M_B are defined as

$$M_k = \frac{3(5-2\beta)\sigma_{tot}^2 R_{eff}}{(3-\beta)G}, \tag{14}$$

$$M_B = \frac{\pi R_{eff}^2 B_{3D}}{\sqrt{\frac{3(3-\beta)}{2(5-2\beta)}\mu_0\pi G}}, \tag{15}$$

where β ranges from 0 (uniform density) to 2 (centrally peaked). The effective radius of each molecular cloud, $R_{eff} = \sqrt{A_{cloud}/\pi}$, is derived from its enclosed area A_{cloud}. Using this framework, we calculate the virial parameter for individual CMZ clouds. The results, listed in Table 1, reveal that nearly all CMZ clouds are supervirial ($\alpha_{k+B} > 1$), except Sgr B2. This suggests that most dense gas in the CMZ is stable against gravitational collapse, consistent with the observed quiescent star formation activity.

Interestingly, despite the diverse and complex evolution of AMs in individual clouds, a general trend emerges: clouds with relatively small virial parameters ($\alpha_{k+B} \lesssim 3$) or high mass-to-flux ratios ($\lambda \gtrsim 1.0$), such as Sgr C, TLP, Cloud E/F, and Sgr B2, tend to show negative AM values in high-density regions. In contrast, clouds with larger virial parameters ($\alpha_{k+B} \gtrsim 4$) or lower mass-to-flux ratios ($\lambda \lesssim 0.8$), such as

50MC and G0.253+0.016, consistently exhibit positive AM values across all density bins. This trend suggests that the evolution of relative orientation between magnetic fields and density structures may be associated with the balance between magnetic, turbulent kinetic, and gravitational energies as the MHD simulations suggested.

4.3. Origin of the Observed Alignment in the CMZ

Several MHD simulations (e.g., J. D. Soler et al. 2013; C.-Y. Chen et al. 2016; J. D. Soler & P. Hennebelle 2017; D. Seifried et al. 2020) explored the origin of the transition of relative orientations between magnetic field and column density structures from parallel to perpendicular with increasing densities and suggested that it is related to the energy balance between magnetic, kinetic, and gravitational energies.

In diffuse, non-self-gravitating regions, velocity shear can stretch both the gas and magnetic field lines in the same direction, producing structures aligned with the field, as shown by P. Hennebelle (2013) and Planck Collaboration et al. (2016a). Similarly, S. Xu et al. (2019) proposed that compressive MHD turbulence can induce mixing that aligns low-density structures in molecular clouds with the local magnetic field. As gas accumulates and becomes denser, a strong magnetic field can restrict gravitational collapse to occur preferentially along the field lines (T. C. Mouschovias 1976), resulting in dense structures oriented perpendicular to the magnetic field. Meanwhile, the supersonic turbulence can generate dense structures in the molecular clouds by shock compression. When turbulence dominates over magnetic forces (super-Alfvénic, $\mathcal{M}_A > 1$), the magnetic field is largely dragged with the gas owing to flux freezing, leading to roughly isotropic compression and field-aligned structures. In contrast, the sub-Alfvénic ($\mathcal{M}_A < 1$) turbulence becomes anisotropic (e.g., S. Sridhar & P. Goldreich 1994; S. Xu et al. 2019), and shocks tend to compress gas along the field lines, producing structures that are preferentially perpendicular to the magnetic field.

According to our HRO analysis, we find that the relative orientations between magnetic fields and density structures in the CMZ are random in low-density bins ($2 \times 10^{22} \lesssim N_{H_2} \lesssim 10^{23}$ cm^{-2}) and parallel at high-density bins ($N_{H_2} \gtrsim 10^{23}$ cm^{-2}). As discussed in Section 3.3, the synthetic observations of MHD simulations show that the random relative orientation in low-density bins can be caused by the projection effects from LOS integrations of unrelated diffuse components since the CMZ is observed in the edge-on perspective. For the parallel alignment observed in the high-density regime, two possible explanations exist: (1) the CMZ has low magnetization, allowing gas motion to drag the magnetic field lines, or (2) most CMZ clouds remain stable against gravitational collapse despite their gas high densities, with strong shear aligning the matter and magnetic field lines. The magnetic field strength in the CMZ is substantially higher than in the Galactic disk, reaching values of $\sim$0.1–1 mG (K. Ferrière 2009; S. N. Longmore et al. 2013; X. Pan et al. 2024). Notably, molecular clouds such as G0.253+0.016 (T. Pillai et al. 2015) and 50MC (X. Lu et al. 2024) exhibit subcritical states, implying that magnetic fields play a dominant role over gravity. These observations suggest that low magnetization is unlikely to be a universal condition for all CMZ clouds. Additionally,

all clouds in our sample except Sgr B2 are supervirial ($\alpha_{k+B} > 1$), meaning that they are not self-gravitating. This supports the second explanation. We also found that in the CMZ dense regions such as Sgr C, Sgr B2, and Cloud E/F exhibit density structures that are perpendicular to the local magnetic field, while also showing relatively weak magnetic fields compared to turbulence ($\mathcal{M}_A \gtrsim 1$). Hence, the shock compression by supersonic turbulence may not be the major factor that causes the dense structures perpendicular to the local magnetic field. We therefore propose that the parallel alignment in the CMZ arises because the majority of its gas remains stable against gravitational collapse, even at high densities, thanks to the additional support provided by strong turbulence and magnetic fields here. Furthermore, in some molecular clouds (e.g., Sgr C, Cloud E/F, and Sgr B2), the magnetic field becomes orthogonal to the column density structures only in regions of exceptionally high density ($\gtrsim 10^{23}$ cm^{-2}). This suggests that significantly more material is required in the CMZ compared to the Galactic disk to overcome support provided by strong turbulence and the magnetic field and trigger gravitational collapse and star formation. This finding is consistent with the observed low star formation efficiency in the CMZ.

5. Summary

We present a study of the relative orientation between magnetic fields in the CMZ from SOFIA/HAWC+ data and column density structures derived by SED fitting of Herschel and ATLASGAL data.

Our study reveals a random alignment in the low-density regime ($10^{22} < N_{H_2} < 10^{23}$ cm^{-2}) and a trend toward parallel alignment at higher densities ($N_{H_2} \gtrsim 10^{23}$ cm^{-2}), in contrast to the typical transition from parallel to perpendicular alignment observed in the Galactic disk with increasing column density. Numerical experiments using MHD simulations of the CMZ suggest parallel alignment in both projected 2D and 3D synthetic observations across all density regimes. This consistency between observations and simulations strongly suggests that the parallel alignment in the CMZ is intrinsic rather than an artifact of projection effects.

We also investigate individual molecular clouds in the CMZ, finding significant variations in the relative orientations between magnetic fields and density structures. In 20MC, 50MC, and G0.253+0.016, nearly all density bins exhibit parallel alignment. In contrast, TLP and Cloud D predominantly show perpendicular alignment. Sgr B2, after recovering its densest regions, displays a transition from parallel to perpendicular alignment, similar to Sgr C. Meanwhile, Cloud E/F undergoes a more complex evolution, shifting from perpendicular to parallel and back to perpendicular alignment as density increases.

Through analysis of the energy balance between magnetic, kinetic, and gravitational components, we find that all CMZ clouds are supervirial despite their high densities—except for Sgr B2, which exhibits a significantly lower virial parameter and more active star formation. This indicates that most dense gas structures in the CMZ are stable against gravitational collapse, supported by strong turbulence and magnetic fields. Such stability explains the origin of parallel alignment observed throughout the CMZ region.

Future studies incorporating higher-resolution polarization data will help reveal the details of relative orientations between magnetic fields and column density structures within individual clouds, particularly for compact, dense structures (e.g., clumps and cores) that are more directly linked to star formation and small clouds (e.g., Dust Ridge Clouds B and C), which are excluded in our analysis owing to a lack of sufficient data points for statistical analysis. Exploring the connection between SFRs and the evolution of relative orientations in these regions will offer new insights into how magnetic field interacts with turbulence and gravity at smaller scales in the CMZ.

Acknowledgments

Appendix A
Dust Temperature Map of the CMZ

The distribution of column density and dust temperature uncertainty in the CMZ.
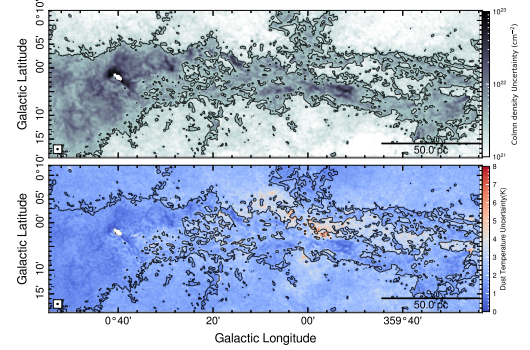

Figure 8. The distribution of column density and dust temperature uncertainty in the CMZ derived by SED fitting in Section 2.2. The black contour marks a column density of 2.0×10^{22} cm^{-2}.

Appendix B
Relative Orientation Plot of Sgr B2

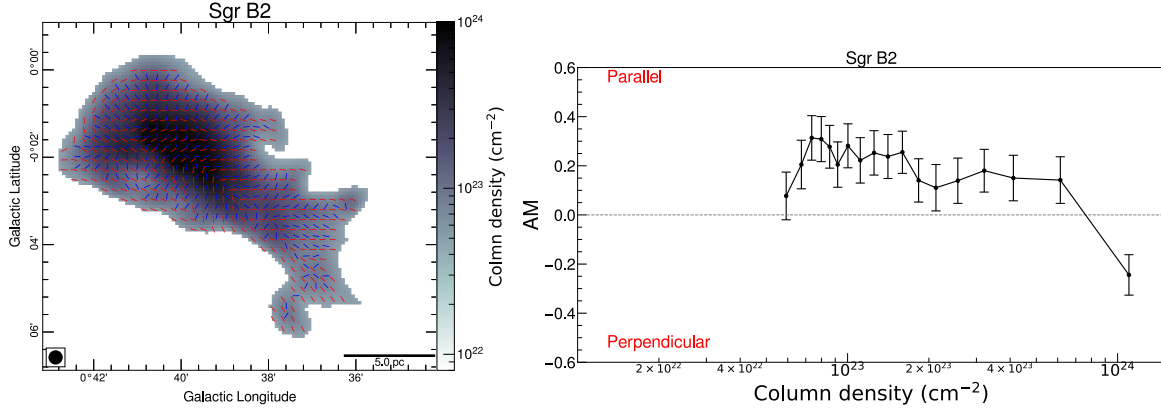Relative orientations of Sgr B2 using 214214 μm SOFIA/HAWC+SOFIA/HAWC+ data.

Figure 9. Relative orientations of Sgr B2 using 214 μm SOFIA/HAWC+ data. Left panel: comparisons between the orientations of magnetic field and column density structure for Sgr B2. The column density map is derived by 214 μm SOFIA/HAWC+ Stokes I emission, recovering the densest regions in Sgr B2. The panel format is the same as for Figure 3. Right panel: alignment measurements for Sgr B2 with the column density derived by 214 μm SOFIA/HAWC+ Stokes I emission.

Appendix C
Fitting Results for ADF Method

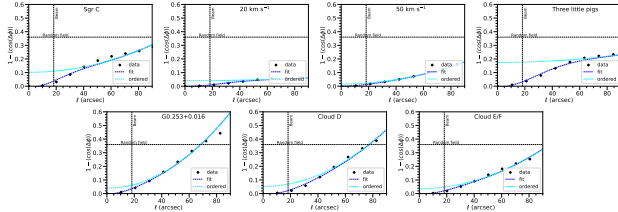Angular dispersion function for individual molecular clouds.

Figure 10. Angular dispersion function for individual molecular clouds. Diamonds represent the angular dispersion segments. The blue dashed line indicates the fitted ADF, while the cyan dashed line represents the ordered component of the best-fit model. The vertical line marks the beam size.

Appendix D
Turbulent Velocity Dispersion

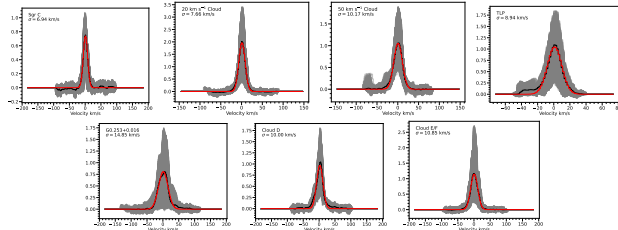HNCO spectra of individual molecular clouds.

Figure 11. HNCO spectra of individual molecular clouds, corrected for local velocities derived from intensity-weighted velocity maps, are presented. Gray lines show the corrected HNCO spectra for all pixels within the coverage of each cloud. The black line indicates the average spectrum, weighted by the integrated intensity of each pixel, while the red line shows the result of the Gaussian fit. The fitted turbulent velocity dispersion is labeled in the upper left corner.

ORCID iDs

Xing Pan ⓘ https://orcid.org/0000-0003-1337-9059
Qizhou Zhang ⓘ https://orcid.org/0000-0003-2384-6589
Keping Qiu ⓘ https://orcid.org/0000-0002-5093-5088
Dylan M. Paré ⓘ https://orcid.org/0000-0002-5811-0136
David T. Chuss ⓘ https://orcid.org/0000-0003-0016-0533
Natalie O. Butterfield ⓘ https://orcid.org/0000-0002-4013-6469
Robin G. Tress ⓘ https://orcid.org/0000-0002-9483-7164
Mattia C. Sormani ⓘ https://orcid.org/0000-0001-6113-6241
Yuping Tang ⓘ https://orcid.org/0000-0002-6581-3307
Steven N. Longmore ⓘ https://orcid.org/0000-0001-6353-0170
Thushara Pillai ⓘ https://orcid.org/0000-0003-2133-4862

References

Barnes, A. T., Longmore, S. N., Battersby, C., et al. 2017, MNRAS, 469, 2263
Battersby, C., Keto, E., Walker, D., et al. 2020, ApJS, 249, 35
Battersby, C., Walker, D. L., Barnes, A., et al. 2025, ApJ, 984, 156
Butterfield, N. O., Chuss, D. T., Guerra, J. A., et al. 2024, ApJ, 963, 130
Chandrasekhar, S., & Fermi, E. 1953, ApJ, 118, 113
Chen, C.-Y., King, P. K., & Li, Z.-Y. 2016, ApJ, 829, 84
Chen, M. C.-Y., Fissel, L. M., Sadavoy, S. I., et al. 2024, MNRAS, 533, 1938
Crutcher, R. M., Nutter, D. J., Ward-Thompson, D., & Kirk, J. M. 2004, ApJ, 600, 279
Csengeri, T., Urquhart, J. S., Schuller, F., et al. 2014, A&A, 565, A75
Davis, L. 1951, PhRv, 81, 890
Demircan, O., & Kahraman, G. 1991, Ap&SS, 181, 313
Etxaluze, M., Goicoechea, J. R., Cernicharo, J., et al. 2013, A&A, 556, A137
Falceta-Gonçalves, D., Lazarian, A., & Kowal, G. 2008, ApJ, 679, 537
Ferrière, K. 2009, A&A, 505, 1183
Fissel, L. M., Ade, P. A. R., Angilè, F. E., et al. 2019, ApJ, 878, 110
Gaume, R. A., Claussen, M. J., de Pree, C. G., Goss, W. M., & Mehringer, D. M. 1995, ApJ, 449, 663
Ginsburg, A., Bally, J., Barnes, A., et al. 2018, ApJ, 853, 171
Girichidis, P. 2021, MNRAS, 507, 5641
Glover, S. C. O., & Clark, P. C. 2012, MNRAS, 426, 377
Goldsmith, P. F., Lis, D. C., Hills, R., & Lasenby, J. 1990, ApJ, 350, 186
Guan, Y., Clark, S. E., Hensley, B. S., et al. 2021, ApJ, 920, 6
Harper, D. A., Runyan, M. C., Dowell, C. D., et al. 2018, JAI, 7, 1840008

Hatchfield, H. P., Battersby, C., Barnes, A. T., et al. 2024, ApJ, 962, 14
Hennebelle, P. 2013, A&A, 556, A153
Henshaw, J. D., Longmore, S. N., Kruijssen, J. M. D., et al. 2016, MNRAS, 457, 2675
Heyer, M., & Dame, T. M. 2015, ARA&A, 53, 583
Hildebrand, R. H., Kirby, L., Dotson, J. L., Houde, M., & Vaillancourt, J. E. 2009, ApJ, 696, 567
Houde, M., Hull, C. L. H., Plambeck, R. L., Vaillancourt, J. E., & Hildebrand, R. H. 2016, ApJ, 820, 38
Houde, M., Vaillancourt, J. E., Hildebrand, R. H., Chitsazzadeh, S., & Kirby, L. 2009, ApJ, 706, 1504
Hu, Y., Lazarian, A., & Wang, Q. D. 2022, MNRAS, 511, 829
Huettemeister, S., Wilson, T. L., Mauersberger, R., et al. 1995, A&A, 294, 667
Hunter, G. H., Sormani, M. C., Beckmann, J. P., et al. 2024, A&A, 692, A216
Huttemeister, S., Wilson, T. L., Henkel, C., & Mauersberger, R. 1993, A&A, 276, 445
Jones, P. A., Burton, M. G., Cunningham, M. R., et al. 2012, MNRAS, 419, 2961
Karoly, J., Ward-Thompson, D., Pattle, K., et al. 2025, ApJL, 982, L22
Kauffmann, J., Pillai, T., & Zhang, Q. 2013, ApJL, 765, L35
Kauffmann, J., Pillai, T., Zhang, Q., et al. 2017, A&A, 603, A89
Kendrew, S., Ginsburg, A., Johnston, K., et al. 2013, ApJL, 775, L50
Kruijssen, J. M. D., Longmore, S. N., Elmegreen, B. G., et al. 2014, MNRAS, 440, 3370
Krumholz, M. R., & Kruijssen, J. M. D. 2015, MNRAS, 453, 739
Kuiper, G. P. 1938, ApJ, 88, 472
Lada, C. J., Lombardi, M., & Alves, J. F. 2010, ApJ, 724, 687
Lazarian, A., & Yuen, K. H. 2018, ApJ, 853, 96
Lis, D. C., & Goldsmith, P. F. 1991, ApJ, 369, 157
Liu, J., Zhang, Q., Commerçon, B., et al. 2021, ApJ, 919, 79
Liu, J., Zhang, Q., Koch, P. M., et al. 2023, ApJ, 945, 160
Liu, J., Zhang, Q., & Qiu, K. 2022, FrASS, 9, 943556
Liu, J., Zhang, Q., Qiu, K., et al. 2020, ApJ, 895, 142
Longmore, S. N., Bally, J., Testi, L., et al. 2013, MNRAS, 429, 987
Longmore, S. N., Rathborne, J., Bastian, N., et al. 2012, ApJ, 746, 117
Lu, X., Liu, J., Pillai, T., et al. 2024, ApJ, 962, 39
Lu, X., Mills, E. A. C., Ginsburg, A., et al. 2019a, ApJS, 244, 35
Lu, X., Zhang, Q., Kauffmann, J., et al. 2015, ApJL, 814, L18
Lu, X., Zhang, Q., Kauffmann, J., et al. 2019b, ApJ, 872, 171
Malinen, J., Montier, L., Montillaud, J., et al. 2016, MNRAS, 460, 1934
Mangilli, A., Aumont, J., Bernard, J. P., et al. 2019, A&A, 630, A74
Mathis, J. S., Mezger, P. G., & Panagia, N. 1983, A&A, 128, 212
Mathis, J. S., Rumpl, W., & Nordsieck, K. H. 1977, ApJ, 217, 425
Mills, E. A. C., & Battersby, C. 2017, ApJ, 835, 76
Molinari, S., Bally, J., Noriega-Crespo, A., et al. 2011, ApJL, 735, L33
Molinari, S., Swinyard, B., Bally, J., et al. 2010, PASP, 122, 314
Morris, M., & Serabyn, E. 1996, ARA&A, 34, 645
Mouschovias, T. C. 1976, ApJ, 206, 753
Myers, P. C., Hatchfield, H. P., & Battersby, C. 2022, ApJ, 929, 34
Nakano, T., & Nakamura, T. 1978, PASJ, 30, 671
Ossenkopf, V., & Henning, T. 1994, A&A, 291, 943
Pakmor, R., Bauer, A., & Springel, V. 2011, MNRAS, 418, 1392
Pakmor, R., & Springel, V. 2013, MNRAS, 432, 176
Pan, X., Zhang, Q., Qiu, K., et al. 2024, ApJ, 972, 30
Paré, D., Butterfield, N. O., Chuss, D. T., et al. 2024, ApJ, 969, 150
Paré, D. M., Chuss, D. T., Karpovich, K., et al. 2025, ApJ, 978, 28
Peter, T., Klessen, R. S., Kanschat, G., Glover, S. C. O., & Bastian, P. 2023, MNRAS, 519, 4263
Pierce-Price, D., Richer, J. S., Greaves, J. S., et al. 2000, ApJL, 545, L121
Pillai, T., Kauffmann, J., Tan, J. C., et al. 2015, ApJ, 799, 74
Planck Collaboration, Adam, R., Ade, P. A. R., et al. 2016a, A&A, 586, A135
Planck Collaboration, Ade, P. A. R., Aghanim, N., et al. 2014, A&A, 571, A1
Planck Collaboration, Ade, P. A. R., Aghanim, N., et al. 2016b, A&A, 586, A138
Qin, S. L., Schilke, P., Rolffs, R., et al. 2011, A&A, 530, L9
Reissl, S., Wolf, S., & Brauer, R. 2016, A&A, 593, A87
Schuller, F., Menten, K. M., Contreras, Y., et al. 2009, A&A, 504, 415
Seifried, D., Walch, S., Weis, M., et al. 2020, MNRAS, 497, 4196
Soler, J. D. 2019, A&A, 629, A96
Soler, J. D., Ade, P. A. R., Angilè, F. E., et al. 2017, A&A, 603, A64
Soler, J. D., & Hennebelle, P. 2017, A&A, 607, A2
Soler, J. D., Hennebelle, P., Martin, P. G., et al. 2013, ApJ, 774, 128
Springel, V. 2010, MNRAS, 401, 791
Sridhar, S., & Goldreich, P. 1994, ApJ, 432, 612
Tang, Y., Wang, Q. D., Wilson, G. W., et al. 2021, MNRAS, 505, 2392
Temi, P., Hoffman, D., Ennico, K., & Le, J. 2018, JAI, 7, 1840011
Tress, R. G., Sormani, M. C., Girichidis, P., et al. 2024, A&A, 691, A303
Tress, R. G., Sormani, M. C., Glover, S. C. O., et al. 2020, MNRAS, 499, 4455
Walker, D. L., Longmore, S. N., Bally, J., et al. 2021, MNRAS, 503, 77
Walker, D. L., Longmore, S. N., Bastian, N., et al. 2015, MNRAS, 449, 715
Walker, D. L., Longmore, S. N., Zhang, Q., et al. 2018, MNRAS, 474, 2373
Weinberger, R., Springel, V., & Pakmor, R. 2020, ApJS, 248, 32
Xu, S., Ji, S., & Lazarian, A. 2019, ApJ, 878, 157
Yang, M.-Z., Lai, S.-P., Karoly, J., et al. 2025, ApJ, 983, 184